



저작자표시-비영리-변경금지 2.0 대한민국

이용자는 아래의 조건을 따르는 경우에 한하여 자유롭게

- 이 저작물을 복제, 배포, 전송, 전시, 공연 및 방송할 수 있습니다.

다음과 같은 조건을 따라야 합니다:



저작자표시. 귀하는 원저작자를 표시하여야 합니다.



비영리. 귀하는 이 저작물을 영리 목적으로 이용할 수 없습니다.



변경금지. 귀하는 이 저작물을 개작, 변형 또는 가공할 수 없습니다.

- 귀하는, 이 저작물의 재이용이나 배포의 경우, 이 저작물에 적용된 이용허락조건을 명확하게 나타내어야 합니다.
- 저작권자로부터 별도의 허가를 받으면 이러한 조건들은 적용되지 않습니다.

저작권법에 따른 이용자의 권리는 위의 내용에 의하여 영향을 받지 않습니다.

이것은 [이용허락규약\(Legal Code\)](#)을 이해하기 쉽게 요약한 것입니다.

[Disclaimer](#)

Master's Thesis

Deterministic Growth Sodium Metal Anode on Pre-
patterned Current Collector for Highly
Rechargeable Seawater Battery

Jaeho Jung

Department of Energy Engineering
(Battery Science and Technology)

Graduate School of UNIST

2020

Deterministic Growth Sodium Metal Anode on
Pre-patterned Current Collector for Highly
Rechargeable Seawater Battery

Jaeho Jung

Department of Energy Engineering
(Battery Science and Technology)

Graduate School of UNIST

Deterministic Growth Sodium Metal Anode on
Pre-patterned Current Collector for Highly
Rechargeable Seawater Battery

A thesis/dissertation
submitted to the Graduate School of UNIST
in partial fulfillment of the
requirements for the degree of
Master of Science

Jaeho Jung

06/02/2020 of submission

Approved by



Advisor

Seok Ju Kang

Deterministic Growth Sodium Metal Anode on Pre-patterned Current Collector
for Highly Rechargeable Seawater Battery

Jaeho Jung

This certifies that the thesis/dissertation of Jaeho Jung is approved.

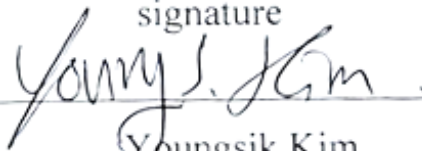
06/02/2020

signature



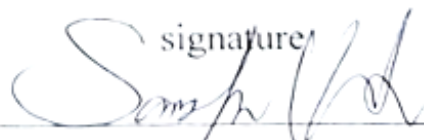
Advisor: Seok Ju Kang

signature



Youngsik Kim

signature



Sang Kyu Kwak

Contents

Abstract.....	6
List of figures.....	7
List of tables.....	10
Chapter 1 Deterministic growth of sodium metal on Cu/Al pre-patterned current collector to control Na dendrite.....	11
1.1 Introduction of metal-based rechargeable batteries.....	11
1.2 The property of Na metal as anode materials and research trends.....	12
1.3 Challenges of Na metal anodes and other's research approach.....	13
1.4 Cu/Al pre-patterned current collector for film-like dendrite growth	14
Chapter 2 Rechargeable Seawater battery using Cu/Al pre-patterned current collector.....	27
2.1 The characteristics of seawater battery.....	27
2.2 Improvement of Seawater battery by applying Cu/Al pre-patterned current collector.....	27
2.3 Experimental section.....	30
2.3.1 Preparation of pre-patterned current collectors.....	30
2.3.2 Materials and cell fabrication.....	30
2.3.3 Morphology characterization.....	30
2.3.4 Electrochemical Characterization.....	31
2.3.5 Computer simulation.....	31
2.4 Conclusions.....	35
References	36

Abstract

Anode-free seawater batteries have emerged as a prospective candidate for next-generation energy-storage cells because of their unique discharge and charge characteristics. To fulfill this promise, reliable Na metal plating on the current collector surface is an important requirement for improving electrochemical properties. Here, we develop a strategy for deterministic growth of Na metal on a pre-patterned current collector. The different surface energies of the Cu and Al metal surfaces enable the growth of patterned Na islands during electrochemical deposition, which efficiently form a film-like layer of Na metal. In particular, determining an optimum ratio between the metal-pattern diameter and the distance between adjacent pattern edges is the critical factor for producing decent Na metal pattern array that can facilitate the enhancement of Coulombic efficiency and cycling capability of a half-cell structure. Moreover, patterned growth of Na metal is highly beneficial to enhancement of the electrochemical performance of seawater batteries. By using a Na super-ionic conductor separator with a Cu/Al pre-patterned current collector, well-patterned growth of Na islands with improved cycling stability for over 200 cycles can be obtained for anode-free seawater battery.

List of figures

Figure 1.1 Dependence of the energy density of a battery cell on the areal capacity of the electrode for Li–air, Li–S, and Li-ion batteries, and the estimated driving distance of an electric vehicle with respect to the energy density of the battery cell used.

Figure 1.2 Natural abundance of Na in the earth’s crust.

Figure 1.3 Various research activities in each field for dendrite growth of metal-based anode: high-surface-area electrodes, artificial layer, smart electrolyte.

Figure 1.4 Schematic illustration of the substrate surface energy (γ_s), crystal surface energy (γ_c), interfacial energy (γ_i), and wetting angle (θ) with two different types of film-growth modes.

Figure 1.5 Galvanostatic plating of Na metal on Au, Ag, Cu, Al, and Ni substrates at a current density of $10 \mu\text{A cm}^{-2}$.

Figure 1.6 (a) From left to right: top and side views of atomic structures of fully relaxed supercells of Au(001)/Na(001), Al(001)/Na(001), Ag(001)/Na(001), Cu(001)/Na(001), and Ni(001)/Na(001) interfaces; the violet, gold, pink, light gray, orange, and blue spheres represent Na, Au, Al, Ag, Cu, and Ni atoms, respectively. (b) Work of adhesion (W_{ad}) (colored bars, left y axis) of the interface between Na and five metal current collectors vs. binding energy (right y axis) of Na atoms on each metal’s (001) surface; W_{ad} of Ni is shown with a variable range (see Supplementary note I, Experiment Section).

Figure 1.7 Model of system for calculating the binding energy of Na on each metal’s (001) surface. The violet, gold, light gray, orange, pink, and blue spheres represent Na, Au, Ag, Cu, Al, and Ni atoms, respectively.

Figure 1.8 (a) Photographs and (b–f) plane-view SEM images of Au, Ag, Cu, Al, and Ni current collectors after plated with 0.1 mAh cm^{-2} Na metal.

Figure 1.9 Schematic procedure for fabricating a Cu/Al pre-patterned current collector.

Figure 1.10 (a) Cross-sectional view SEM image of Cu/Al pre-patterned current collector. (b) Magnified SEM image of dash-dot square region in (a).

Figure 1.11 (a–c) SEM images of Na metal plating on a Cu/Al pre-pattern at a current 0.5 mA; the Na ions were first plated on Cu, and they merged with adjacent Na islands. (d)

Galvanostatic plating of Na metal on a Cu/Ag pre-patterned current collector; the inset shows a schematic of Na islands on a Cu/Ag pre-pattern.

Figure 1.12 Top view SEM images and corresponding EDX elemental mapping of Al, Cu, and Na for a (a) bare Cu/Al pre-pattern and (b) 0.15 mA h Na plated Cu/Al pre-pattern.

Figure 1.13 (a) SEM micrograph of a plated Na island array on a Cu/Al pre-patterned current collector with a λ value of 0.5; the inset shows the ratio of metal-pattern diameter (r) to distance (d) between edges of adjacent patterns. SEM images of plated Na islands on (b) triangular, (c) square, and (d) pentagonal pre-patterned current collectors with a λ value of 0.5. SEM micrographs of plated Na metal on a Cu/Al pre-pattern with λ values of (e) 1.5 and (f) 2.0. (g) Plot of pattern fraction vs. λ value from 0.5 to 2.0.

Figure 1.14 Plane-view SEM images of SUS masks with (a) circular, (b) triangular, (c) square, and (d) pentagonal patterns.

Figure 1.15 Histograms of pattern fraction of Na metal islands versus various pre-patterned current collectors shown in Table 1.

Figure 1.16 (a) Galvanostatic plating and stripping on pre-patterned current collectors with λ values of 0.5 to 2.0 and pristine Cu and Al current collectors. (b) Zoomed-in image of galvanostatic plating at the 30th, 120th, and 290th cycles. (c) Coulombic efficiency of pre-patterned current collectors ($\lambda = 0.5-2.0$) and pristine Cu and Al current collectors as a function of cycle number. (d) Rate performance of Cu/Al pre-patterned current collectors with a λ value of 0.5 in the current density range of 0.5 to 3 mA cm⁻².

Figure 1.17 Galvanostatic plating and stripping on pre-patterned current collectors ($\lambda = 1$) with 1 M NaClO₄-DME (blue), 1 M NaOTf-DME (gray), and 1 M NaPF₆-DME (red) electrolytes.

Figure 1.18 Post-mortem SEM images of pre-patterned Cu/Al current collectors with λ values of (a) 0.5, (b) 1, (c) 1.5, (d) 2, (e) pristine Cu, and (f) Al current collector after cycling tests of 2032-type coin cells.

Figure 1.19 Nyquist plots of the impedance spectra for Cu/Al patterns with λ value range of 0.5-2.0 at the 15th cycle.

Figure 2.1 (a) Schematic illustration of a seawater battery consisting of a Cu/Al pre-patterned current collector, NASICON ceramic separator, and seawater cathode. SEM micrographs of plated Na islands on a NASICON separator using (b) circular, (c) triangular, and (d) square pre-patterned current collectors; the insets of (c) and (d) show the SEM images of pre-patterned Cu/Al current collectors. (e) Rate performance of the Cu/Al pre-patterned current collector

with a λ value of 0.5 and the pristine Cu current collector, the pre-patterned current collector and pristine Cu current collector are represented by the red and black lines, respectively; the insets show zoomed-in snapshots of the 50th, 100th, and 200th galvanostatic cycles. (f) Coulombic efficiency of pre-patterned current collectors with a λ value of 0.5 to 2.0 and pristine Cu current collector as a function of cycle number.

Figure 2.2 (a) Rate performance and (b) corresponding Coulombic efficiency of Cu/Al pre-patterned current collector containing seawater battery in the current density range of 1 to 3 mA cm⁻².

Figure 2.3 Plane-view SEM images of (a) NASICON and (b) pristine Cu foil surfaces with Cu foil after 57 cycles.

Figure 2.4 Surface models of Na, Au, Ag, Cu, Al, and Ni current collectors with (001), (101), and (111) surfaces.

Figure 2.5 Surface energy of (001), (101), and (111) surfaces of pure metal systems.

Figure 2.6 Island growth of Na metal deposition on Ni metal surface. γ_{Ni} is the surface energy of Ni metal (substrate), γ_{Na} is the surface energy of Na metal (crystal), and $\sigma_{\text{Na/Ni}}$ is the interfacial energy of the Na/Ni interface.

List of tables

Table 1 Pattern fraction of Na metal islands on various pre-patterned current collectors.

Chapter 1

1. Deterministic growth of sodium metal on Cu/Al pre-patterned current collector to control Na dendrite

1.1 Introduction of metal-based rechargeable batteries

Li-ion batteries (LIBs) researches made many developments and possibilities in not only portable electronic devices but also personal vehicles. Despite the highest theoretical capacity (3,860 mAh g⁻¹, or 2,061 mAh cm⁻³) and lowest electrochemical potential (-3.04 V versus the standard hydrogen electrode) of Li metal, LIBs have limitation of capacity for fast-charging industrial structures. Therefore, there are many researches for next-generation batteries for high-capacity storage such as Li-S and Li-O₂ as presented Figure 1.1. They have attracted much attention in various electronic devices, such as personal transportation devices, drones, electric vehicles, and energy storage systems (ESS), because of their enormous energy capacity mainly arising from the alkali metal anodes. With tremendously increasing use of Li-ion

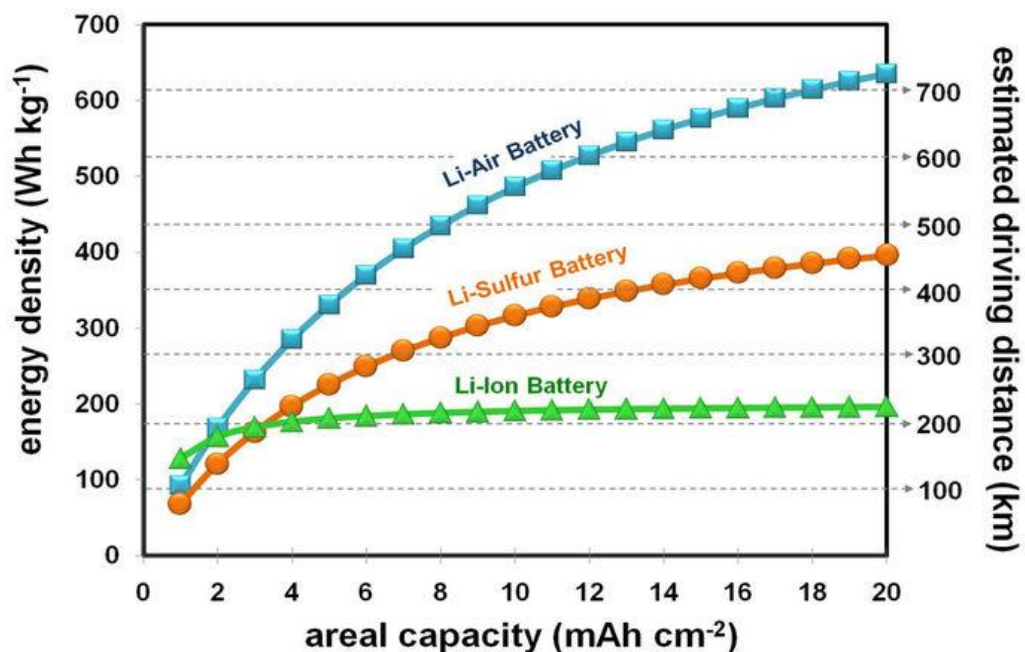


Figure 1.1 Dependence of the energy density of a battery cell on the areal capacity of the electrode for Li-air, Li-S, and Li-ion batteries, and the estimated driving distance of an electric vehicle with respect to the energy density of the battery cell used.

batteries (LIBs) in electric vehicles, their key raw material, Li metal, has become a prized commodity because the market price of LIBs strongly depends on the cost of lithium in the rare-metals market.¹ Although Bolivia, Argentina, and Chile, known as the “Lithium Triangle,” continue to increase the lithium-mining capacity, Australian investment bank Macquarie estimates said that, by 2020, the Li demand will reach 260,000 tons, outstripping the predicted supply of 237,000 tons, which will be problematic for LIB production.²

1.2 The property of Na metal as anode materials and research trends

As an alternative to LIBs, batteries based on sodium ions have attracted much attention because the natural abundance of sodium in the earth’s crust allows us to produce cost-effective energy-storage cells without resource constraints as shown Figure 1.2.³ Among the proposed Na-based energy-storage candidates including Na–O₂ batteries, Na-ion batteries (NIBs), and Na-based capacitors, the seawater battery consisting of a Na metal anode, a Na super-ionic conductor (NASICON) ceramic separator, and a seawater cathode has emerged as the most promising next-generation Na-based battery because of not only the abundant supply of sodium for the anode, but also the endless supply of seawater as the cathode material.⁴⁻¹²

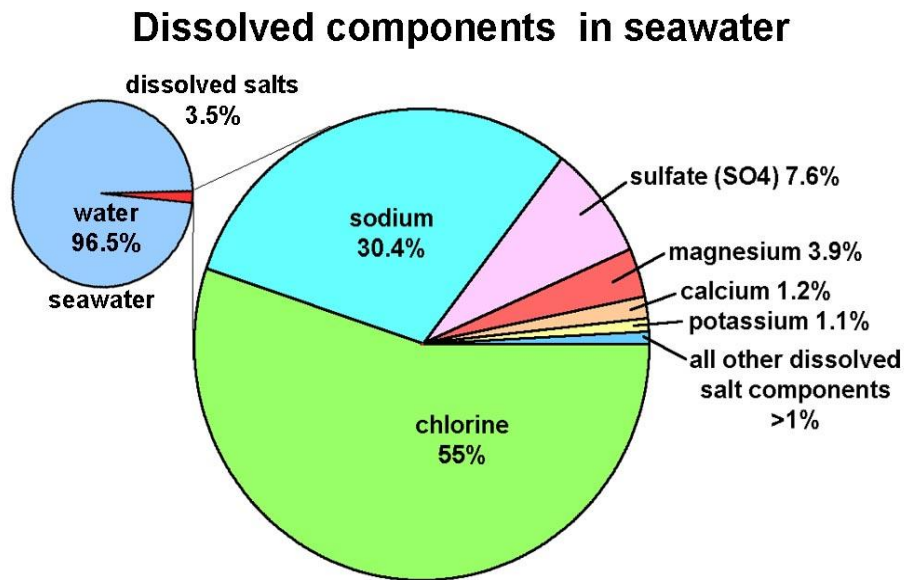


Figure 1.2 Natural abundance of Na in the earth’s crust.

1.3 Challenges of Na metal anodes and other's research approach

After the successful demonstration of a prototype seawater battery by Kim and co-workers, the carbon current collector on the cathode side was found to be an important component for improving battery performance, leading to intensive studies on materials for the cathode current collector and the subsequent proof of the merits of functional carbon materials.^{9,10,13-16} However, despite the decent electrochemical performance demonstrated by smart cathode materials such as N-doped carbon, hierarchically structured composites of graphene and carbon nanotubes with Co, and bifunctional electrocatalytic carbon sponge, the stability of Na metal anodes should be confirmed to avoid safety issues and increase the cycle life of anode-free seawater batteries.^{13,15,16} To date, the biggest challenge of Na metal anodes is the dendrite formation during the battery cycle because the reactive nature of the alkali metal inevitably generates detrimental dendrite growth, resulting in short circuits that ultimately erode the cell performance.¹⁷⁻²¹ In order to prevent the growth of alkali metal dendrites, substantial efforts have been made using a combination of high-surface-area electrodes, an artificial layer, and a smart electrolyte, which seems to be effective in a conventional alkali-metal-based battery (Figure 1.3).²²⁻³⁷ However, a unique feature of anode-free seawater battery should be considered current collector interface because Na metal is plated on the surface of the bare current collector in every cycle.⁹ Therefore, our group recently investigated the effect of the current collector surface on seawater battery performance.¹⁰ We speculated that the

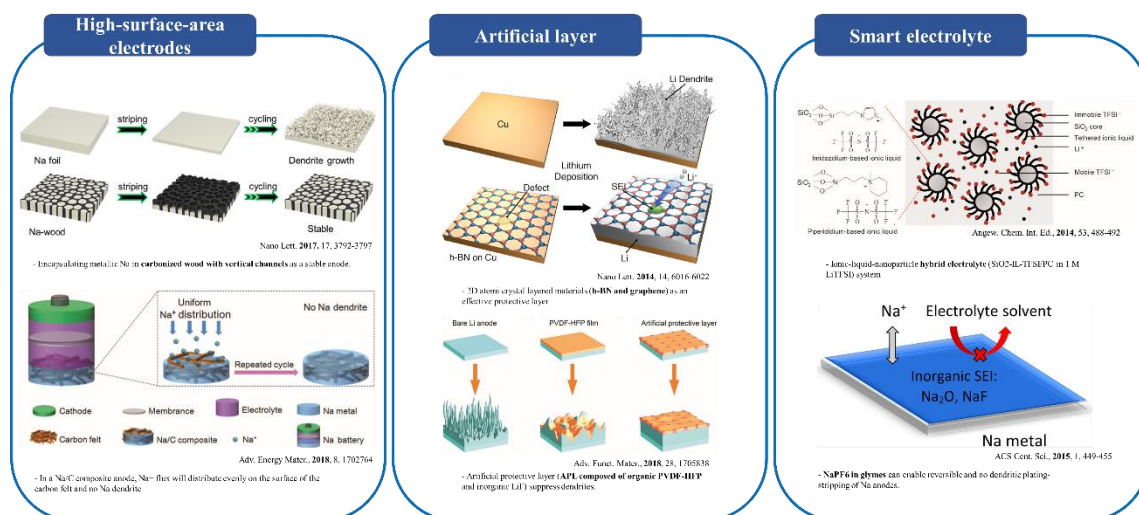


Figure 1.3 Various research activities in each field for dendrite growth of metal-based anode: high-surface-area electrodes, artificial layer, smart electrolyte.

deactivation of a Cu current collector with a single layer of graphene would enable us to improve the electrochemical performance, and we confirmed that modifying the surface of the current collector can enhance the performance of a seawater battery.¹⁰ Despite our recent results showing the effect of a homogeneous current collector surface, randomly generated Na nuclei can turn into the seeds of dendrite growth during the erratic coalescence of Na islands, in turn deteriorating the cell performance.

1.4 Cu/Al pre-patterned current collector for film-like dendrite growth

Here, we present, for the first time, the effect of deterministic growth of Na metal on a pre-patterned current collector of a highly rechargeable seawater battery. We found that the Na ions that are preferentially deposited on the metal surface with relatively high binding energy enable us to produce patterned plating on the current collector. In particular, the ratio between the metal-pattern diameter and the distance between the edges of adjacent patterns is an important factor for successful growth of a Na metal pattern over a large area. With an optimum pattern ratio of 0.5, we obtained promising cycling capability and decent Coulombic efficiency, indicating that patterned Na metal plating is a key parameter for improving electrochemical performance. Furthermore, patterned Na metal growth on the current collector makes the anode-free seawater battery more desirable. The notably enhanced Coulombic efficiency and cycling stability clearly imply that patterned Na metal growth is a promising strategy for

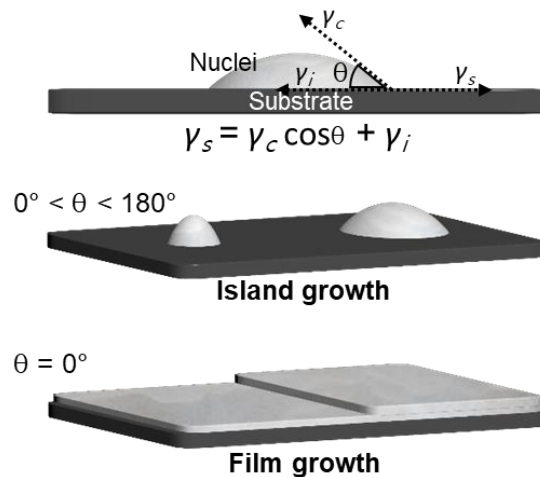


Figure 1.4 Schematic illustration of the substrate surface energy (γ_s), crystal surface energy (γ_c), interfacial energy (γ_i), and wetting angle (θ) with two different types of film-growth modes.

fabricating high-performance anode-free batteries.

Figure 1.4 shows two different types of conventional film-growth modes on a target substrate. Unique growth modes such as the island growth and film growth can be identified by the Young equation of $\gamma_s = \gamma_c \cos\theta + \gamma_i$, where γ_s is the substrate surface energy, γ_c is the surface energy of the crystal, γ_i is the interfacial energy, and $\cos\theta$ is wetting angle.³⁸ For instance, when the γ_s is bigger than the total sum of $\gamma_c \cos\theta$ and γ_i , the growth follows the film growth mode. The island growth mode is observed when $\gamma_s < \gamma_c \cos\theta + \gamma_i$. In general, the growth of alkali Li metal on a current collector is in the island growth, indicating that Li metal grows with an island-like morphology on the current collector as a result of the capillarity of homogeneous nucleation.^{39,40} Thus, voids are inevitably formed between these non-uniformly generated Li islands, resulting in a rough morphology during the erratic coalescence, which leads to dendrite formation. In order to mitigate the detrimental dendrite formation, recently, Cui and co-workers successfully demonstrated that the Li solubility in target substrates plays a critical role in the formation of Li crystals with film-like morphology during electrochemical plating.⁴¹ The key finding of this research was when the target substrate has the same crystal structure and similar atomic radii as those of Li, the target substrate such as the case of Au, Ag, and Mg substrates, a Li metal alloy phase tends to be formed at the interface between the current collector and Li metal, which reduces the over potential during Li plating. In particular, the

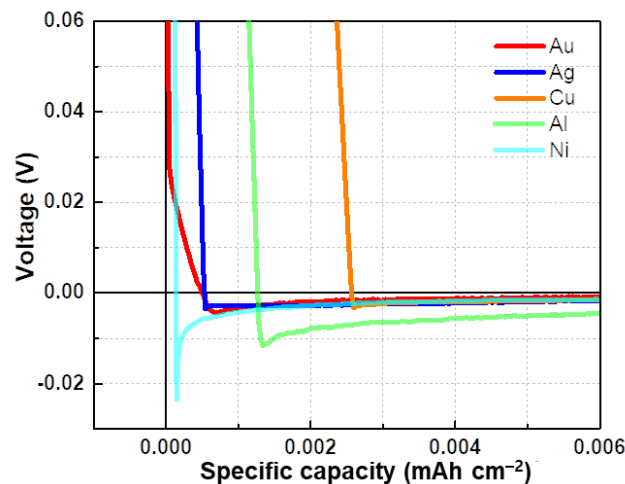


Figure 1.5 Galvanostatic plating of Na metal on Au, Ag, Cu, Al, and Ni substrates at a current density of $10 \mu\text{A cm}^{-2}$.

selectively plated Li metal on an Au surface suggests that monitoring Na metal plating on various metal substrates is the first step in controlling the growth mode of Na metal.

Figure 1.5 shows the galvanostatic profiles of Na metal plating on Au, Ag, Cu, Al, and Ni current collectors. As clearly seen in the plots, the plating trajectory strongly depends on the current collector material. For example, Au exhibited the lowest plating overpotential, while Ni showed the highest plating resistance. The different galvanostatic characteristics indirectly revealed that the Na metal growth mode varied with on different current collector surfaces. A theoretical study was also conducted to investigate the trends of Na plating on each metal substrate (Au, Ag, Cu, Al, and Ni) that were observed in the experiment. Density functional theory (DFT) calculation was used to examine the interfacial stability of Na metal and various current collectors (see “Computer simulation” in Experiment Section). The interface systems considered were Na metal with the (001) surface and (001) surface of each metal substrate (Au, Ag, Cu, Al, and Ni). We modeled a total of five interface systems (Figure 1.6a) and five Na-adsorption systems on each metal (Figure 1.7). To investigate the interface stability of the interface systems, the work of adhesion (W_{ad}) and binding energy (E_b) were examined. W_{ad} is defined as the energy required to separate two surfaces from one another; the higher the W_{ad} value, the higher the interfacial strength. In conjunction with the growth model scheme, W_{ad} provides detailed study on the interfacial stability by assessing both substrate and crystal surface energy, as well as interfacial energy as part of interface formation energy.

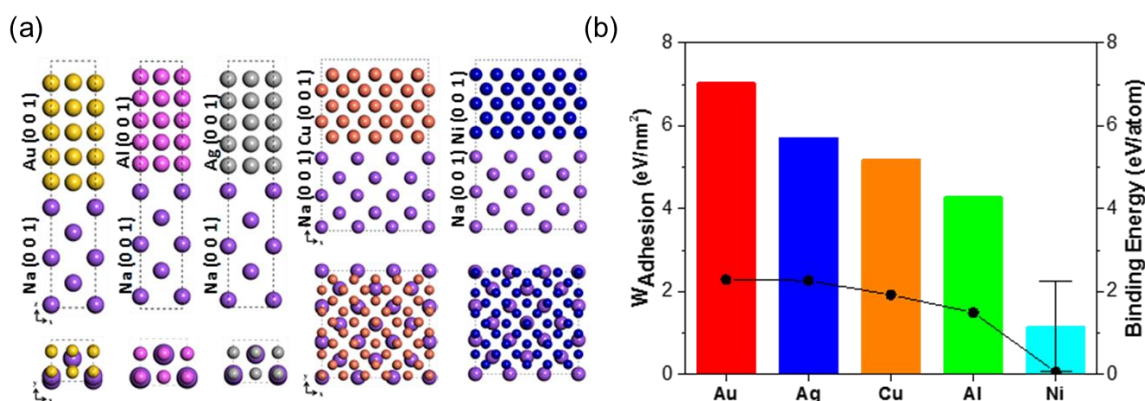


Figure 1.6 (a) From left to right: top and side views of atomic structures of fully relaxed supercells of Au(001)/Na(001), Al(001)/Na(001), Ag(001)/Na(001), Cu(001)/Na(001), and Ni(001)/Na(001) interfaces; the violet, gold, pink, light gray, orange, and blue spheres represent Na, Au, Al, Ag, Cu, and Ni atoms, respectively. (b) Work of adhesion (W_{ad}) (colored bars, left y axis) of the interface between Na and five metal current collectors vs. binding energy (right y axis) of Na atoms on each metal’s (001) surface; W_{ad} of Ni is shown with a variable range (see Supplementary note 1, Experimental Section).

The interface models with high interfacial stability among the surfaces of each metal substrate were Na(001)/Au(001), Na(001)/Ag(001), and Na(001)/Cu(001), as shown in Figure 1.6b. Based on the calculated W_{ad} values, the Na/Au interface has the highest work of adhesion, which implies that it has the strongest interface, followed by the Na/Ag interface, Na/Cu interface, Na/Al interface, and Na/Ni interface whose results are well matched with nucleation potential in Figure 1.5. Similarly, the calculated E_b values show that Na/Au interface has the highest binding energy, which suggests that it is the most probable adsorption site for Na plating. The E_b value decreases in the order of Na/Ag interface > Na/Cu interface > Na/Al interface > Na/Ni interface. In particular, W_{ad} of the Ni current collector is reported within certain possible range here instead of well as interfacial energy as part of interface formation energy. The interface models with high interfacial stability among the surfaces of each metal substrate were Na(001)/Au(001), Na(001)/Ag(001), and Na(001)/Cu(001), as shown in Figure 1.6b. Based on the calculated W_{ad} values, the Na/Au interface has the highest work of adhesion, which implies that it has the strongest interface, followed by the Na/Ag interface, Na/Cu

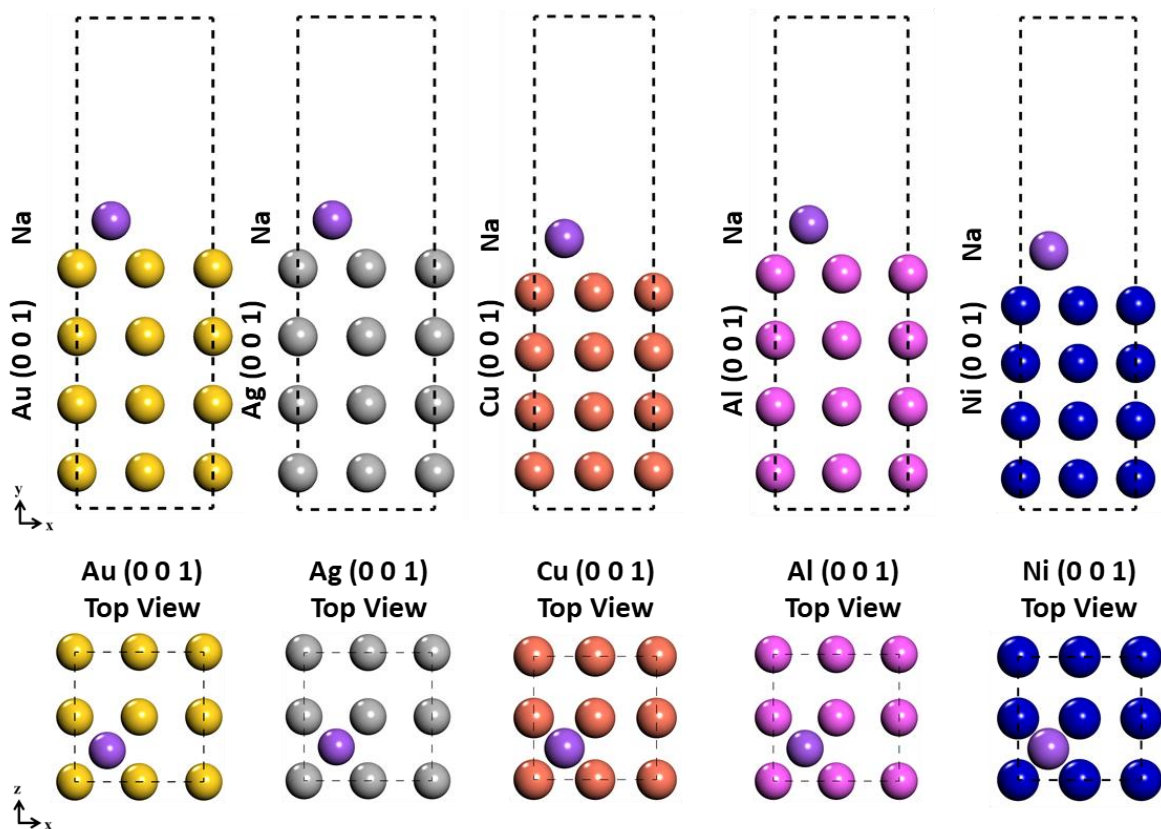


Figure 1.7 Model of system for calculating the binding energy of Na on each metal's (001) surface. The violet, gold, light gray, orange, pink, and blue spheres represent Na, Au, Ag, Cu, Al, and Ni atoms, respectively.

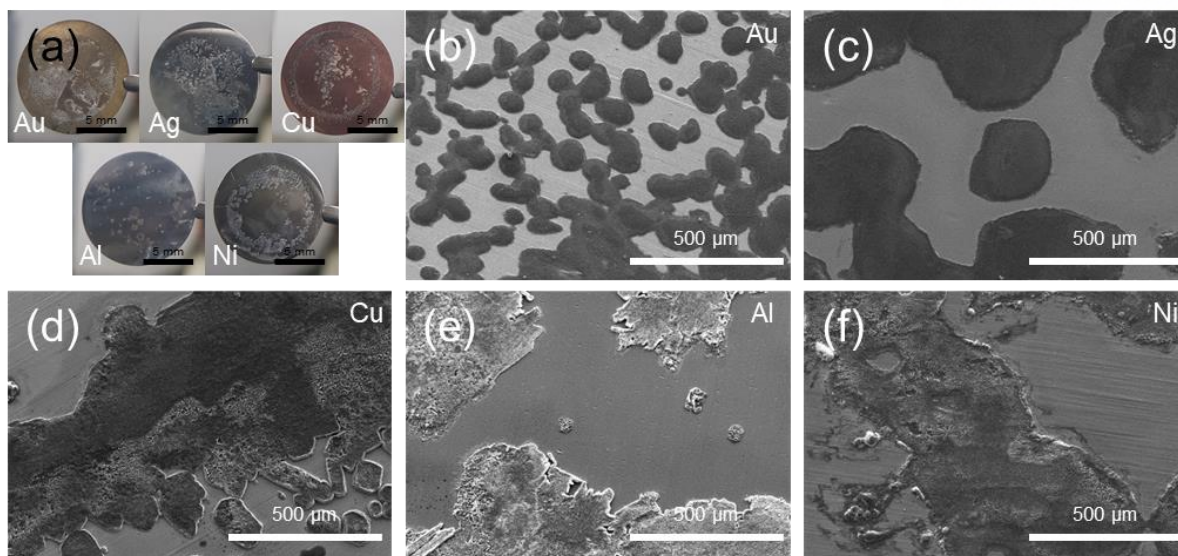


Figure 1.8 (a) Photographs and (b–f) plane-view SEM images of Au, Ag, Cu, Al, and Ni current collectors after plated with 0.1 mA h cm^{-2} Na metal.

interface, Na/Al interface, and Na/Ni interface whose results are well matched with nucleation potential in Figure 1.5. Similarly, the calculated E_b values show that Na/Au interface has the highest binding energy, which suggests that it is the most probable adsorption site for Na plating. The E_b value decreases in the order of Na/Ag interface > Na/Cu interface > Na/Al interface > Na/Ni interface. In particular, W_{ad} of the Ni current collector is reported within certain possible range here instead of an exact value because Na metal deposition on the Ni surface naturally adopts the island-like growth model (see Supplementary Note I in the Experimental Section). These results confirm the experimental findings of Au, Cu, and Ag current collectors showing high Na plating tendency, while Al and Ni current collectors had low Na plating tendency. However, the plated Na metal (0.1 mA h cm^{-2}) morphology on the Au current collector clearly showed randomly distributed Na islands despite the galvanostatic profile and theoretical prediction film growth of Na on the Au surface (Figure 1.8). Thus, it is reasonable to hypothesize that the Na metal always forms island-like deposits regardless of the substrate material, which ultimately erode the cell performance, suggests that controlling the Na islands is critical for high quality Na metal plating on a current collector.

To examine the deterministic growth of Na islands on a current collector, we introduced pre-patterned metal substrates to guide the Na metal plating because the galvanostatic results (Figure 1.5) suggest that Na ions were preferentially deposited on a metal surface with relatively high binding energy. In addition, it is reasonable to speculate that the Ni–Au pre-

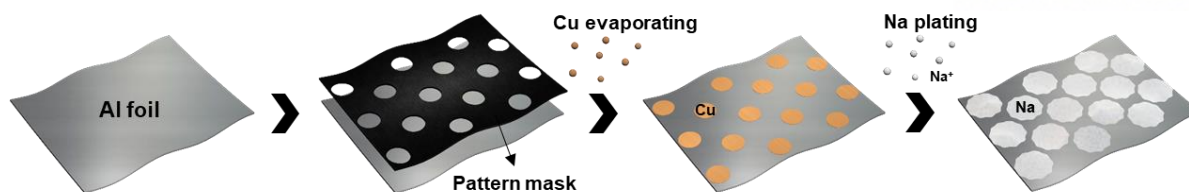


Figure 1.9 Schematic procedure for fabricating a Cu/Al pre-patterned current collector.

patterned substrate was the best combination for forming the patterned Na metal plating on a current collector. However, owing to the cost-ineffective Au, we selected the Al–Cu pre-pattern for our investigation. Figure 1.9 presents a Cu/Al pre-patterned current collector prepared by thermal evaporation of approximately 100 nm thick Cu metal on Al foil through chemically etched SUS (stainless steel) masks (Figure 1.10). The well-defined circular Cu pattern with diameter of 250 μm was characterized by scanning electron microscopy (SEM). In order to plate the Na metal on the pre-patterned current collector, we applied a galvanostatic current of 0.5 mA (0.325 mA cm^{-2} for 17 min), and 1 M sodium trifluoromethanesulfonate (NaOTf) in dimethyl ether (DME) was used as an electrolyte. The effect of the pre-patterned current collector was successfully visualized by the distinctive patterned growth of Na metal. The SEM images in Figure 1.11a and 1.11b clearly show that the Na ions first plate on the boundary of Al and Cu and progressively filled the Cu region, which agree with previous observations of selective Li_2S deposition of edge sites in a MoS_2 nanosheet.⁴² After further deposition of Na metal on the Cu/Al pre-patterned current collector, the adjacent Na islands on the Cu regions merged to form a film-like aggregate, which is one of the desired growth modes for mitigating dendrite formation (Figure 1.11c). It should be noted that since the limited solubility of Na in Cu, the Na element dominantly appears in the energy dispersive X-

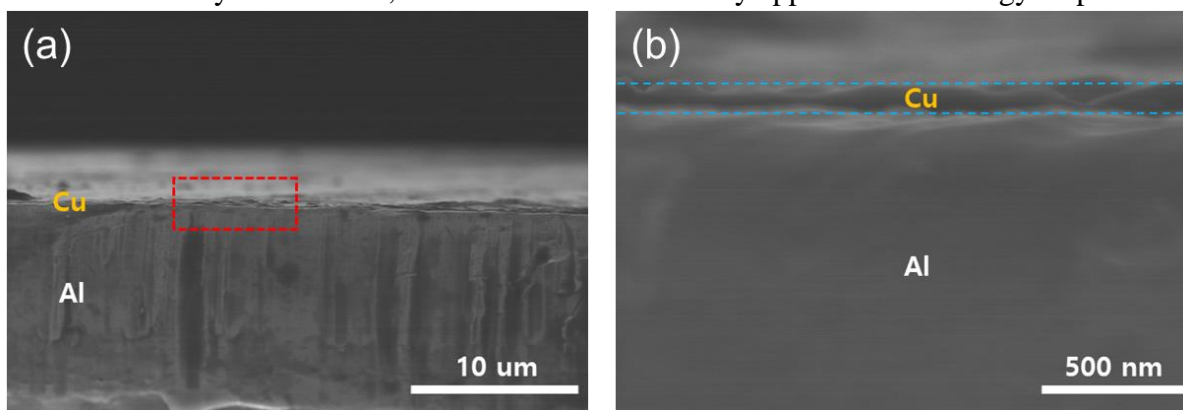


Figure 1.10 (a) Cross-sectional view SEM image of Cu/Al pre-patterned current collector. (b) Magnified SEM image of dash-dot square region in (a).

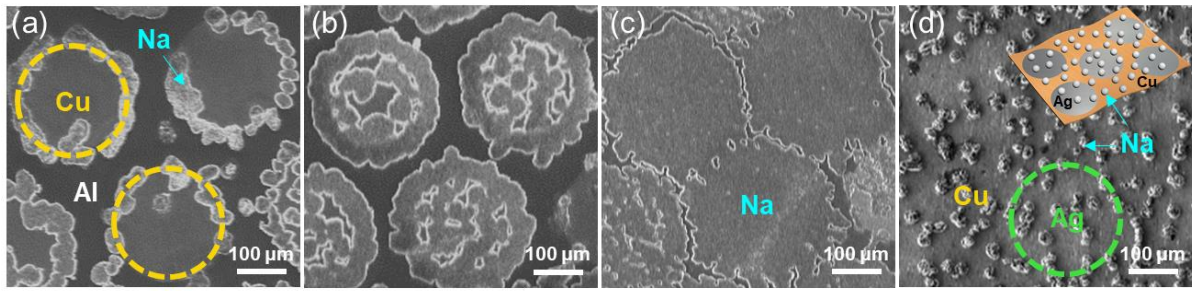


Figure 1.11 (a-c) SEM images of Na metal plating on a Cu/Al pre-pattern at a current 0.5 mA; the Na ions were first plated on Cu, and they merged with adjacent Na islands. (d) Galvanostatic plating of Na metal on a Cu/Ag pre-patterned current collector; the inset shows a schematic of Na islands on a Cu/Ag pre-pattern.

ray (EDX) mapping of plated Na on the Cu/Al pre-pattern (Figure 1.12).⁴³ In particular, this result implies the main driving force for growing the patterned Na metal was the relative W_{ad} and difference between E_b of Cu (5.19 eV nm^{-2} and $1.92 \text{ eV atom}^{-1}$) and Al (4.29 eV nm^{-2} and $1.49 \text{ eV atom}^{-1}$) metals on the current collector. As shown in the earlier DFT calculation results of the current collector with a Cu pattern on Al surface, Na plating on the Cu metal surface was much preferred owing to the difference between W_{ad} and E_b of the Na/Cu and the Na/Al interface systems. When Na metal plating was used for a pattern of metals with relatively similar W_{ad} and E_b , for example Cu (5.19 eV nm^{-2} and $1.92 \text{ eV atom}^{-1}$) and Ag (5.70 eV nm^{-2} and $2.27 \text{ eV atom}^{-1}$), we observed random nucleation of Na metal on the pre-patterned Cu/Ag current collector, indicating that the larger W_{ad} difference and smaller E_b are the prerequisites for patterned growth of Na metal (Figure 1.11d).

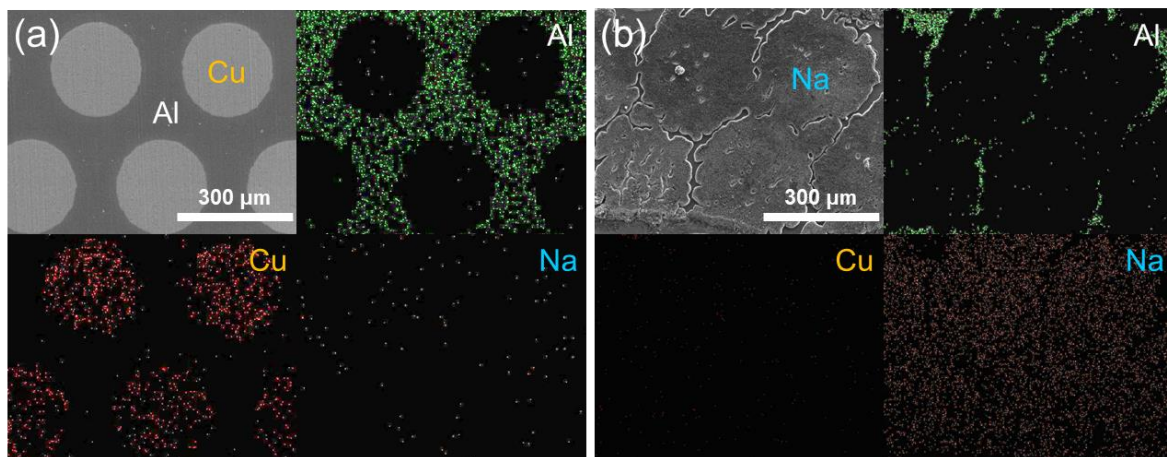


Figure 1.12 Top view SEM images and corresponding EDX elemental mapping of Al, Cu, and Na for a (a) bare Cu/Al pre-pattern and (b) 0.15 mA h Na plated Cu/Al pre-pattern.

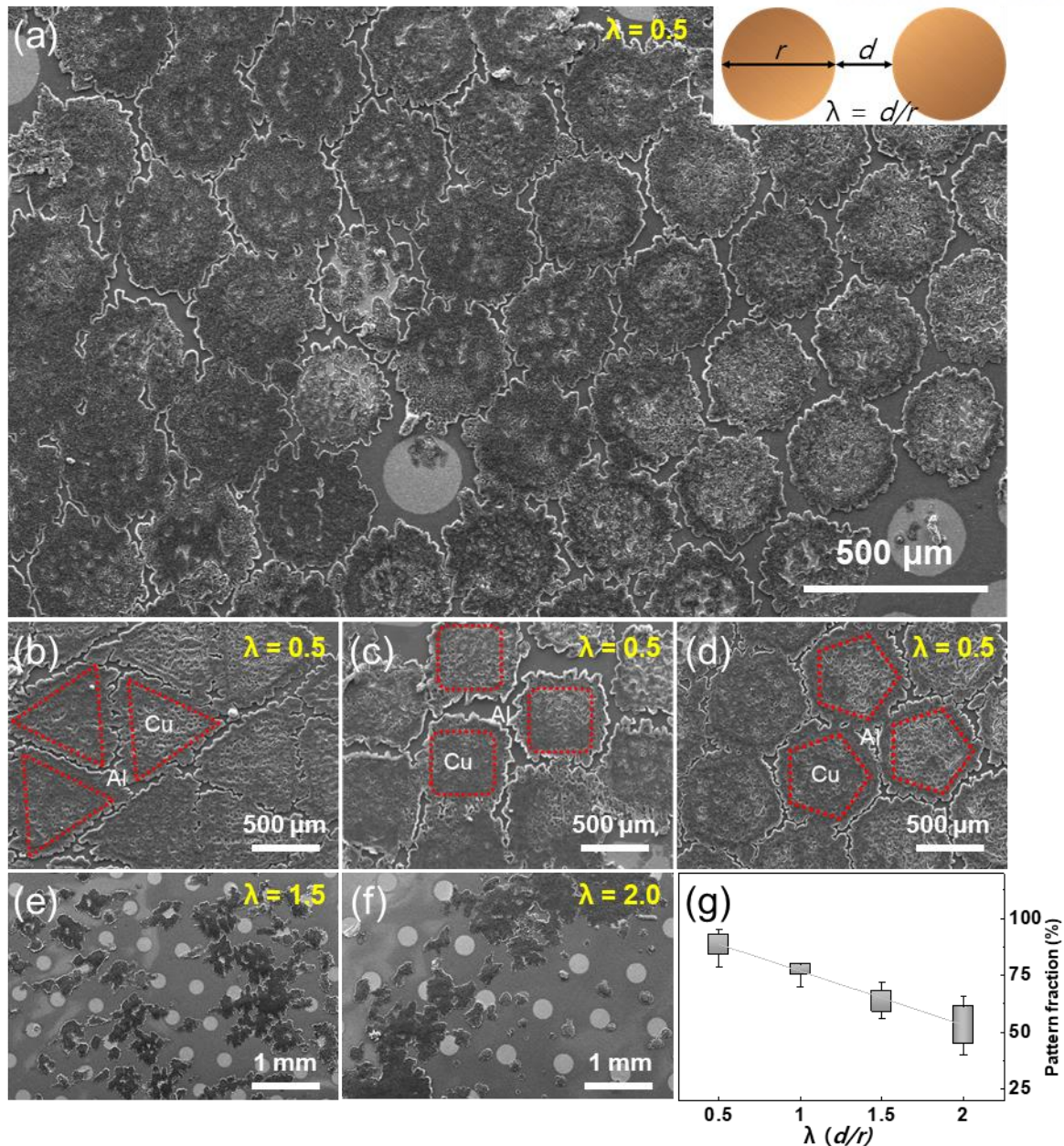


Figure 1.13 (a) SEM micrograph of a plated Na island array on a Cu/Al pre-patterned current collector with a λ value of 0.5; the inset shows the ratio of metal-pattern diameter (r) to distance (d) between edges of adjacent patterns. SEM images of plated Na islands on (b) triangular, (c) square, and (d) pentagonal pre-patterned current collectors with a λ value of 0.5. SEM micrographs of plated Na metal on a Cu/Al pre-pattern with λ values of (e) 1.5 and (f) 2.0. (g) Plot of pattern fraction vs. λ value from 0.5 to 2.0.

In order to find the optimum condition for Na metal growth on the Cu/Al pre-patterned current collector, we investigated the effect of pattern size and length of periodicity. We introduced a new value λ , which is the ratio between metal-pattern diameter and the distance between adjacent pattern edges, as shown in the inset of Figure 1.13. The λ values systematically varied from 0.5 to 2.0 in the Cu circular pattern on the Al current collector. As

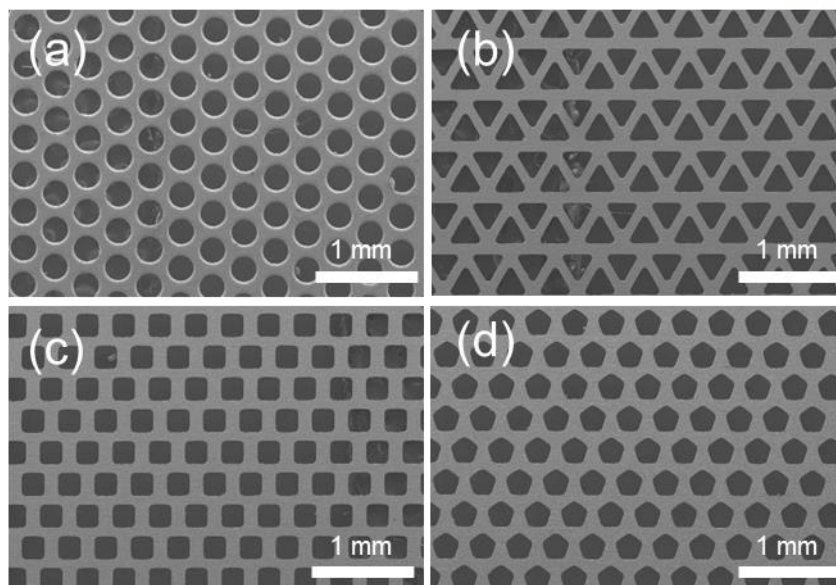


Figure 1.14 Plane-view SEM images of SUS masks with (a) circular, (b) triangular, (c) square, and (d) pentagonal patterns.

shown in the SEM image (Figure 1.13a), when the λ value was 0.5, globally well-patterned Na metal islands formed on the Cu/Al pre-patterned current collector, where the Na metal islands were dominant on the Cu region with relatively high binding energy, regardless of pattern shape (triangle, square, or pentagon) (Figure 1.13b–d and 1.14). In particular, the results indicate that the pattern fraction of Na metal on the current collector was strongly related to the λ . As shown in Figure 1.13e and 1.13f, the pattern fraction decreased with increasing λ , ranging from 90% for λ of 0.5 to ~60% for λ of 2.0 (Figure 1.15 Table 1). These results also clearly indicate that the guided pattern distance played a critical role in attaining a satisfactory Na island pattern array. Although we observed the defects in the SEM image (Figure 1.13a), the λ range of 0.5–1.0 preferentially generated the patterned Na metal plating over a large area (Figure 1.13g), which may enhance the electrochemical performance as a result of the homogenous plating of Na metal on the current collector.

To further confirm the electrochemical performance of the patterned Na metal plating, we employed a 2032-type coin cell consisting of Na metal, a polymeric separator, a current collector, and 1 M NaOTf in DME electrolyte for monitoring the Coulombic efficiency of the pre-patterned current collectors. We applied a galvanostatic current of 1 mA (0.65 mA cm^{-2}

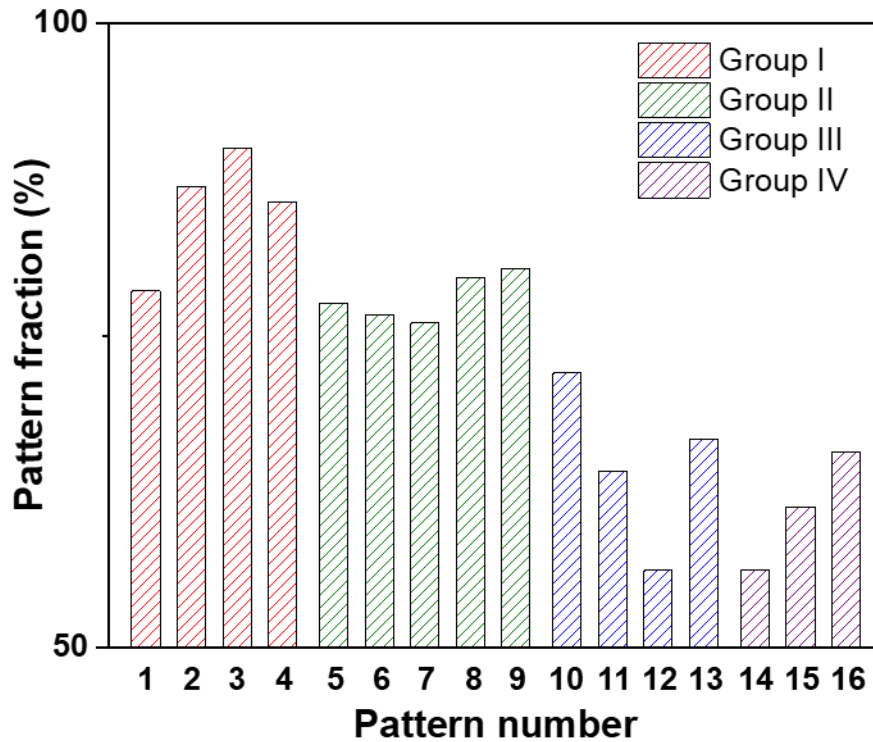


Figure 1.15 Histograms of pattern fraction of Na metal islands versus various pre-patterned current collectors shown in Table 1.

for 33 min) with a 0.5 V potential cutoff for the stripping process. Figure 1.16a shows the cycle life of pristine Cu, pristine Al and Cu/Al pre-patterned current collectors as a function of λ (0.5–2.0). We observed the highest number of cycles for the cycling capability from the pre-patterned current collectors with λ of 0.5, which agrees with the condition for globally well-patterned Na islands (Figure 1.13a). We also noted that the electrochemical performance can be further improved by NaPF₆ in DME electrolyte (Figure 1.17).³⁶ In addition, the magnified plots in Figure 1.16b suggest the nucleation and plating potentials obtained when $\lambda = 0.5$ were

	Group I				Group II					Group III				Group IV		
Pattern #	1	2	3	4	5	6	7	8	9	10	11	12	13	14	15	16
Pattern diameter (r) [μm]	150	200	250	300	100	150	200	250	300	100	200	250	300	200	250	300
Pattern distance (d) [μm]	100	100	125	150	100	150	200	250	300	150	300	375	450	400	500	600
λ [d/r]	0.66	0.5	0.5	0.5	1	1	1	1	1	1.5	1.5	1.5	1.5	2	2	2
Pattern fraction [%]	78.6	86.9	90	85.7	77.6	76.7	76	79.7	80.4	72	64.1	56.2	66.7	56.2	61.3	65.7

^{a)} Pattern fraction = (Number of Na deposited patterns / Number of total pre-patterns) × 100

Table 1 Pattern fraction of Na metal islands on various pre-patterned current collectors.

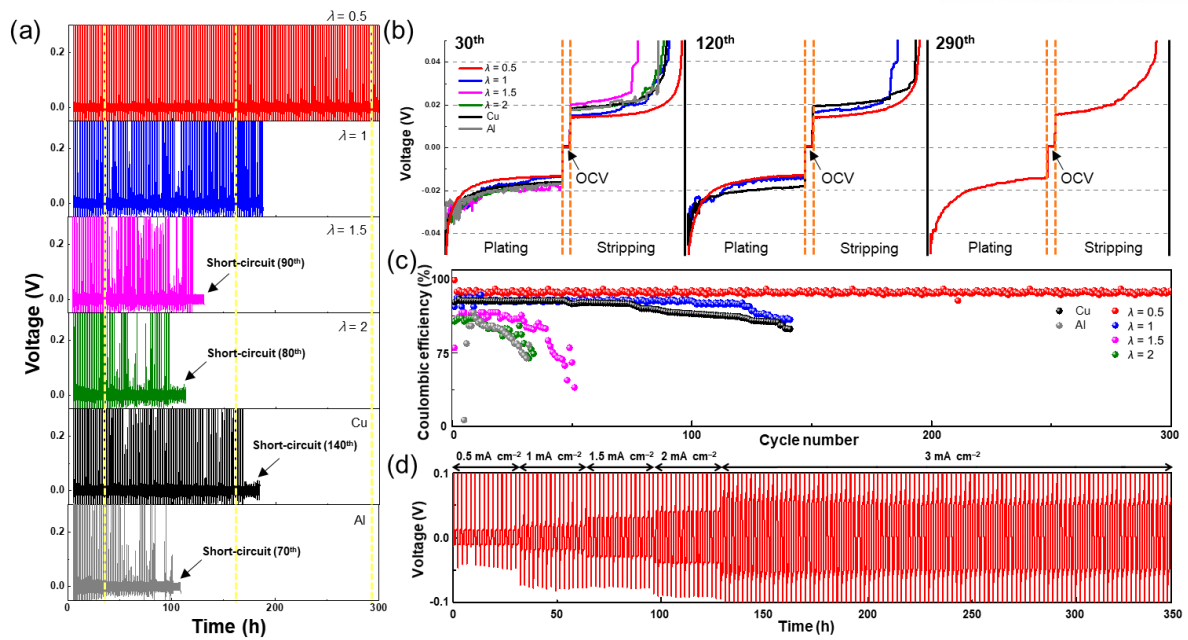


Figure 1.16 (a) Galvanostatic plating and stripping on pre-patterned current collectors with λ values of 0.5 to 2.0 and pristine Cu and Al current collectors. (b) Zoomed-in image of galvanostatic plating at the 30th, 120th, and 290th cycles. (c) Coulombic efficiency of pre-patterned current collectors ($\lambda = 0.5-2.0$) and pristine Cu and Al current collectors as a function of cycle number. (d) Rate performance of Cu/Al pre-patterned current collectors with a λ value of 0.5 in the current density range of 0.5 to 3 mA cm⁻².

almost constant during the cycle and were successfully sustained for over 300 cycles, which is in contrast to the λ values of >1.0 and the pristine metal current collectors including Al, Cu and our previous study of graphene covered Cu substrates. It should be noted that since the number of cycles for pristine Cu was higher than that for pristine Al in Figure 1.16a, the Cu surface was more favorable for enhancing the cycling capability. However, the cycling endurance of current collectors with $\lambda = 0.5$ was significantly higher than that of the pristine Cu current collector, the pre-patterned current collector can be expected to be a more dominant and critical

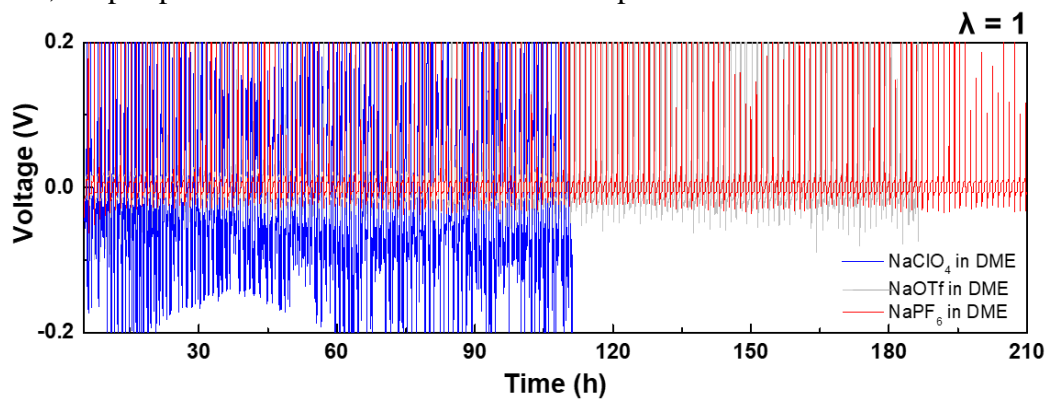


Figure 1.17 Galvanostatic plating and stripping on pre-patterned current collectors ($\lambda = 1$) with 1 M NaClO₄-DME (blue), 1 M NaOTf-DME (gray), and 1 M NaPF₆-DME (red) electrolytes.

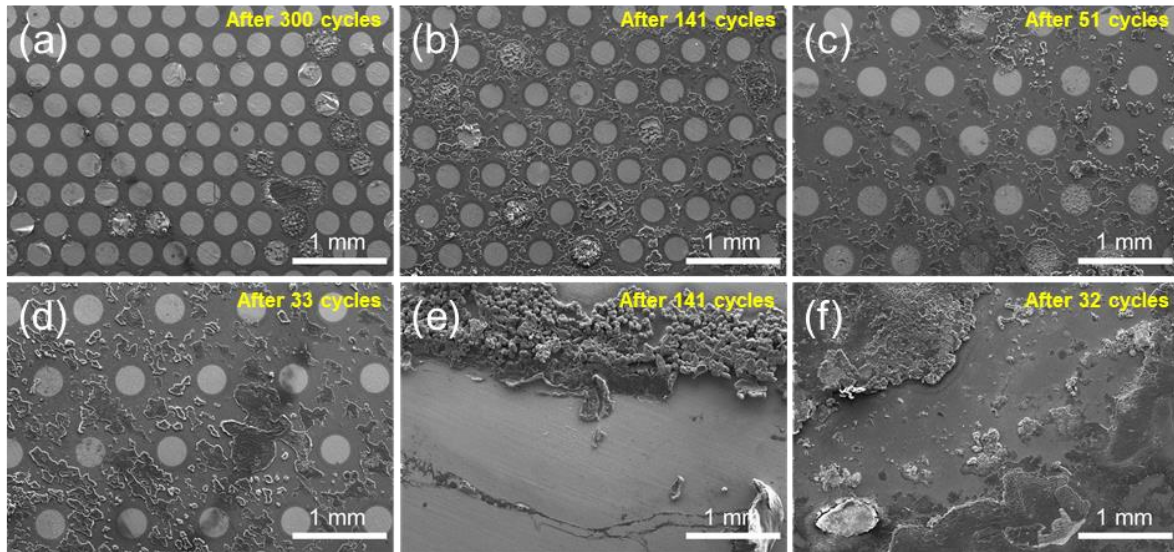


Figure 1.18 Post-mortem SEM images of pre-patterned Cu/Al current collectors with λ values of (a) 0.5, (b) 1, (c) 1.5, (d) 2, (e) pristine Cu, and (f) Al current collector after cycling tests of 2032-type coin cells.

factor for enhancing the cyclability. In addition, the plots of Coulombic efficiency in Figure 1.16c for the current collectors with $\lambda = 0.5$ show a maximum Coulombic efficiency of 95%, and it decreased with increasing λ . The eroding Coulombic efficiency and post-mortem SEM images indicate the strong relationship between λ and the electrochemical performance, which are also matched with EIS measurement (Figure 1.18 and 1.19). Furthermore, we monitored

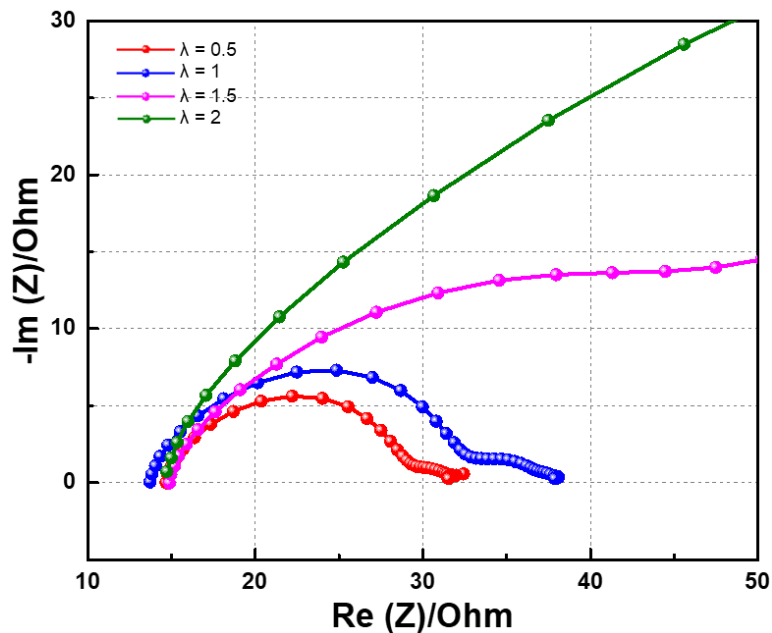


Figure 1.19 Nyquist plots of the impedance spectra for Cu/Al patterns with λ value range of 0.5-2.0 at the 15th cycle.

the rate capability of Cu/Al pre-patterned current collectors with $\lambda = 0.5$ in the current density range of 0.5–3 mA cm⁻². As shown in Figure 1.16d, highly stable plating and stripping cycles were obtained in the voltage–time curves, revealing that the deterministic growth of Na metal efficiently enhanced the electrochemical stability.

Chapter 2

2 Deterministic growth of sodium metal on Cu/Al pre-patterned current collector to control Na dendrite

2.1 The characteristics of seawater battery

Techniques for storing electrical energy through renewable energy are becoming increasingly important : demand for electrical energy, gradual increase in oil prices, depletion of fossil fuels, and the generation of CO₂, the cause of global warming. Most of the eco-friendly energy comes from wind, geothermal and solar power. However, eco-friendly energy has many difficulties in terms of cost and efficiency for direct use. As such, efficient electrical energy storage systems that can store large quantities can be a solution to solve problems and provide energy efficiently in terms of environment and fuel. Sodium-based batteries are focused on many areas, starting with sodium ion batteries. In addition, due to its abundant sodium reserves, it is inexpensive and has good electrical properties as an anode material. Recently, studies on sodium-based water batteries have been actively conducted. Seawater batteries that store energy by using NaCl, an infinite resource of seawater, are receiving a lot of attention in the world. The system is equipped with a system that uses seawater as the electrolyte of the cathode and selectively charges only the sodium ion through the anode. Therefore, it is necessary to construct a system in which seawater and organic electrolytes coexist using a solid membrane different from existing ion batteries, and the correlation of the components should be adjusted to the seawater battery system. In a seawater battery system, too, there is a need to suppress the growth of sodium dendrite in the anode for reversible reactions, which must solve the hazardous and radically degraded efficiency. In addition to solving the problems of the anode part, there is a problem to be solved such as a cathode, a separator, and an electrolyte solution in order to develop a high seawater battery, but a great development is expected due to a lot of research and development.

2.2 Improvement of Seawater battery by applying Cu/Al pre-patterned current collector

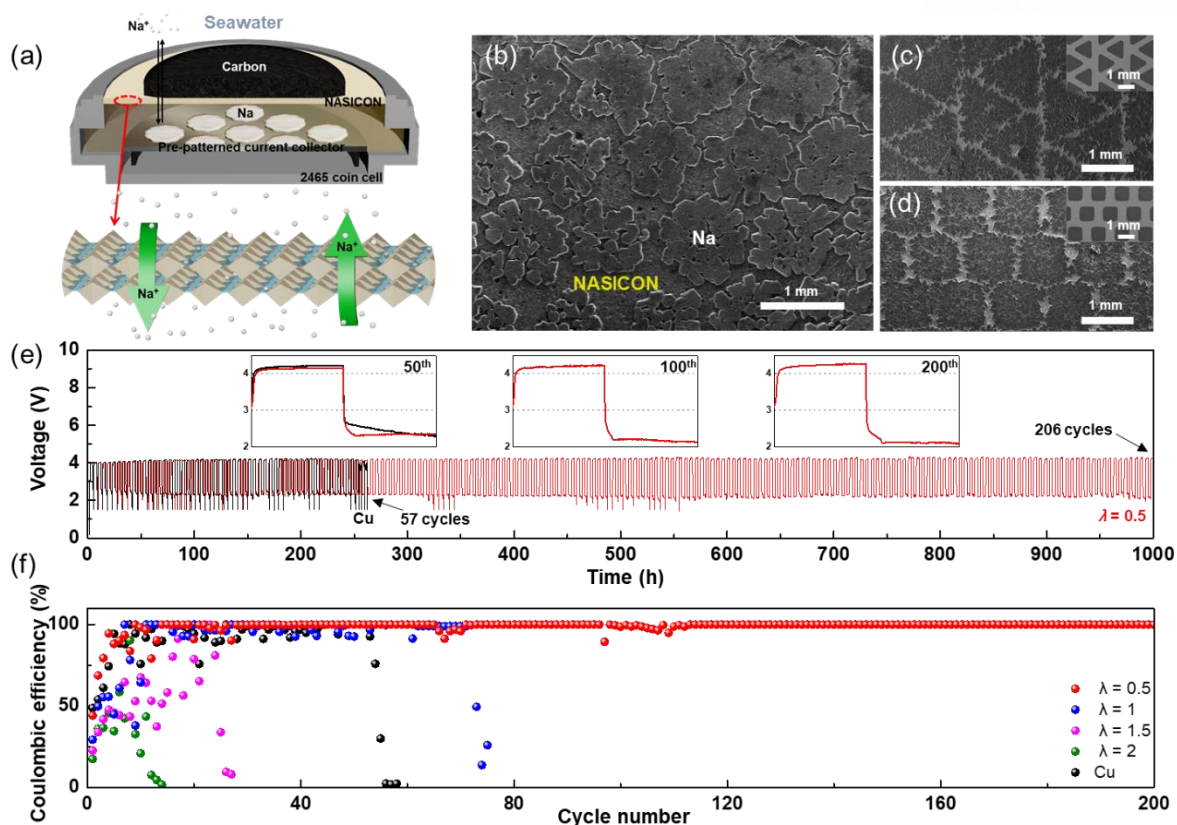


Figure 2.1 (a) Schematic illustration of a seawater battery consisting of a Cu/Al pre-patterned current collector, NASICON ceramic separator, and seawater cathode. SEM micrographs of plated Na islands on a NASICON separator using (b) circular, (c) triangular, and (d) square pre-patterned current collectors; the insets of (c) and (d) show the SEM images of pre-patterned Cu/Al current collectors. (e) Rate performance of the Cu/Al pre-patterned current collector with a λ value of 0.5 and the pristine Cu current collector, the pre-patterned current collector and pristine Cu current collector are represented by the red and black lines, respectively; the insets show zoomed-in snapshots of the 50th, 100th, and 200th galvanostatic cycles. (f) Coulombic efficiency of pre-patterned current collectors with a λ value of 0.5 to 2.0 and pristine Cu current collector as a function of cycle number.

The effect of Na metal growth on Cu/Al pre-patterned current collectors was further evaluated by using a rechargeable seawater battery consisting of a NASICON ceramic separator and 1 M NaOTf in DME electrolyte (Figure 2.1a). It should be noted that the unique structure of the anode-free seawater battery in Figure 2.1a suggests that Na metal was always plated on the exposed current collector surface after it was fully stripped during the discharge process.¹¹ Prior to measuring the electrochemical characteristics of the pre-patterned current collector, we performed SEM investigation after Na metal was deposited at a current of 0.5 mA (0.325 mA cm⁻² for 300 min) on the Cu/Al pre-patterned current collectors with $\lambda = 0.5$. The resulting images in Figure 2.1b-d show the well-developed arrays of circular, triangular, and square Na islands on the NASICON separator, which are similar to previous results shown

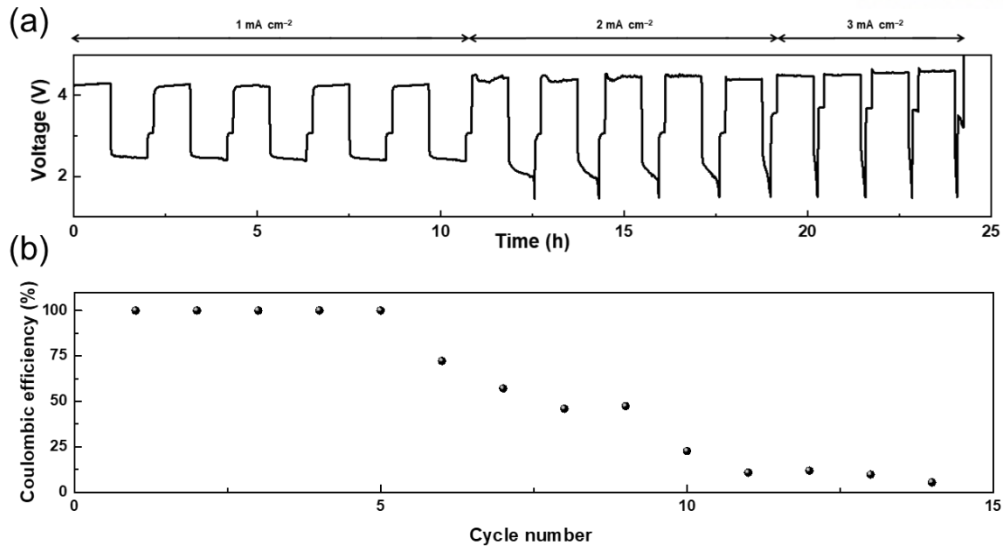


Figure 2.2 (a) Rate performance and (b) corresponding Coulombic efficiency of Cu/Al pre-patterned current collector containing seawater battery in the current density range of 1 to 3 mA cm⁻².

in Figure 1.13. However, unlike the 2032-type coin-cell test, the Na metal islands were physically detached from the pre-patterned current collector and transferred onto the NASICON separator during the disassembly of the cell. One of the plausible reasons was that W_{ad} between NASICON and the Na metal was higher than that of the interface between the Na metal and current collector. As shown in Figure 2.1e, electrochemical performances of a pristine Cu current collector and a Cu/Al pre-patterned current collector with $\lambda = 0.5$ were evaluated by discharging and charging the cells at a constant current of 0.5 mA (0.325 mA cm⁻² for 150 min). Although the performance of the seawater battery was altered by high current densities due to the ionic conductance of the NASICON separator and surface functional groups of the carbon cathode (Figure 2.2), the Cu/Al pre-patterned current collector maintained a Coulombic efficiency of 98% for over 200 cycles, which is approximately four times higher

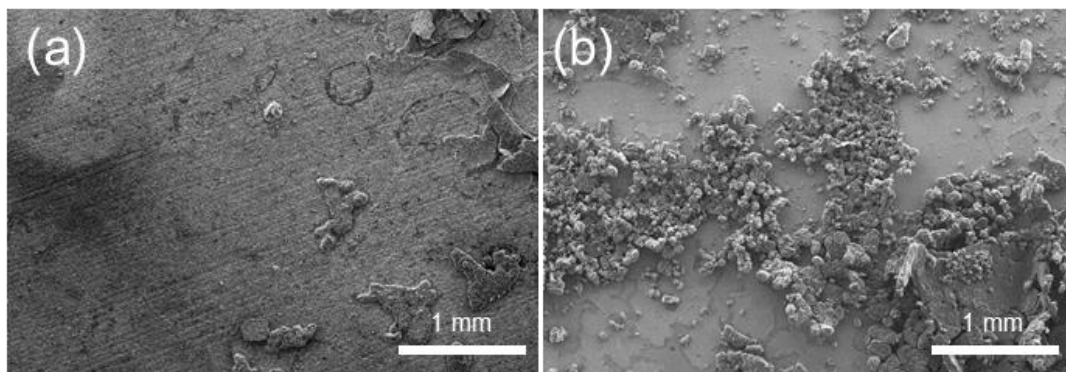


Figure 2.3 Plane-view SEM images of (a) NASICON and (b) pristine Cu foil surfaces with Cu foil after 57 cycles.

than that of pristine Cu current collector (Figure 2.1f and 2.3).^{10,44} The number of cycles recorded for the pristine Cu current collector suggests that deterministic growth of Na metal is an important factor for improved seawater battery performance, and it is a viable method for anode-free battery architecture.

2.3 Experimental section

2.3.1 Preparation of Pre-patterned Current collectors

Pieces of ~20 μm thick Cu and Al foils (99.8%) were used as substrates. The pre-patterned current collectors were fabricated by thermal evaporator under the pressure of 10^6 Torr with an evaporation rate of ~0.1 nm s⁻¹ using a chemically etched shadow SUS masks. Au, Ag, Cu, Ni (99%, Sigma-Aldrich, USA), and Al pellets (99%, ITASCO, Korea) were used as the metal sources for the physical vapor deposition.

2.3.2 Materials and Cell Fabrication

The 2032-type coin cell (Wellcos Co., Korea) and modified 2465-type coin cell were used to characterize the electrochemical performance of Na metal plating and stripping.⁴⁵ Sodium trifluoromethanesulfonate (NaOTf, 98%, Sigma-Aldrich) and polymeric separator (2400, Celgard) were fully dried at 50 °C for 12 h under high vacuum. The 2032-type coin cells were fabricated by using a pre-patterned current collector, polymeric separator, 1 M NaOTf in dimethyl ether (DME, 99.5%, Sigma-Aldrich) electrolyte, and Na foil. For seawater battery assembly, modified 2465-type coin cells were used with Na-super ionic conductor (NASICON, Na₃Zr₂Si₂PO₁₂, 4 TO ONE Energy Co., Korea) separator and 1 M NaOTf in DME electrolyte.⁴⁵ Electrochemical experiments were performed by using a flow-cell structure (4 TO ONE Energy Co., Korea) with the 4 mm thick carbon felt current collector (XF30A, Toyobo, Japan).

2.3.3 Morphology Characterization

The 2032-type coin cell and 2465-type coin cell were disassembled in the Ar-filled glove box (< 0.1 ppm O₂ and H₂O) to examine their post-mortem surface morphologies. The disassembled Na-plated current collectors and NASICON were sealed in an Ar-filled glass vial in glove box to transfer the SEM antechamber (S-4800, Hitachi High-Technologies, Japan) for the surface characterization.

2.3.4 Electrochemical Characterization

Electrochemical experiments were performed using a WBCS3000 battery tester (Wonatech, Korea). The assembled 2032-type coin cells and seawater battery cells were galvanostatically cycled at various current densities. The Coulombic efficiency was calculated as $Q_{\text{stripping}} / Q_{\text{plating}} \times 100\%$, where $Q_{\text{stripping}}$ – Q_{plating} refer to the charge–discharge capacity of the 2032-type coin cell, and discharge–charge capacity of the seawater battery.

2.3.5 Computer simulation

Modeling and Energy Calculations

Density functional theory (DFT) calculations were carried out using a computer program, Cambridge Serial Total Energy Package (CASTEP), to elucidate the dependence of Na metal plating on the surface of various current collectors.⁴⁶ First, we calculated the surface energy of the (001), (101), and (111) surfaces of each metal as shown in Figure 2.4. Based on the calculated values (Figure 2.5), the surface energy of the (111) surfaces are noticeably much higher than those of the (001) and (101) surfaces. Thus, we finalized our interface candidates to the (001) and (101) surfaces. Between these two surfaces, the (001) surface shows the lowest

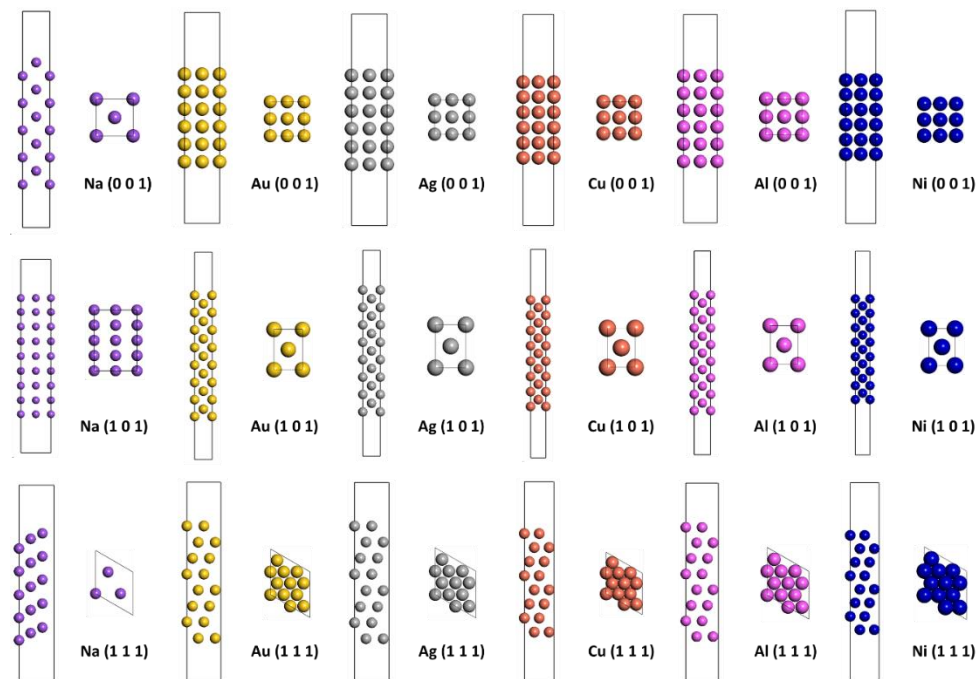


Figure 2.4 Surface models of Na, Au, Ag, Cu, Al, and Ni current collectors with (001), (101), and (111) surfaces.

lattice mismatch across all metal current collector interfaces with Na; therefore, we constructed five interfaces between Na and each metal current collector based on its (001) surface (Figure 1.6a). The in-plane strain to match the two parts in the interface structure was kept below 5%. Generalized gradient approximation (GGA) with the Perdew–Burke–Ernzerhof (PBE) functional was adopted for all calculations.⁴⁷ The ultrasoft pseudopotential was used to treat unreactive core electrons, and the energy cutoff was set to 550 eV.⁴⁸ The Broyden–Fletcher–Goldfarb–Shanno (BFGS) algorithm and Two-Point Steepest Descent (TPSD) algorithm were used for optimization of the geometry of the bulk systems and interface systems, respectively.^{49,50} The convergence thresholds for geometry optimization and SCF density convergence were 1×10^{-5} eV atom⁻¹ and 1×10^{-6} eV atom⁻¹, respectively. The convergence precision of geometry optimization for the maximum force, displacement, and maximum stress were set to 0.03 eV Å⁻¹, 0.001 Å, and 0.05 GPa, respectively. For optimization of the bulk structure, a Monkhorst–Pack *k*-point mesh was used, and it was set to $12 \times 12 \times 12$ for the bulk unit cell of Na, Au, Ag, Cu, Al, and Ni.⁵¹

The energy calculations employed in the study were adopted from the calculations carried out by Liu. et al., and Wang et al.; modifications were made before we carried out our

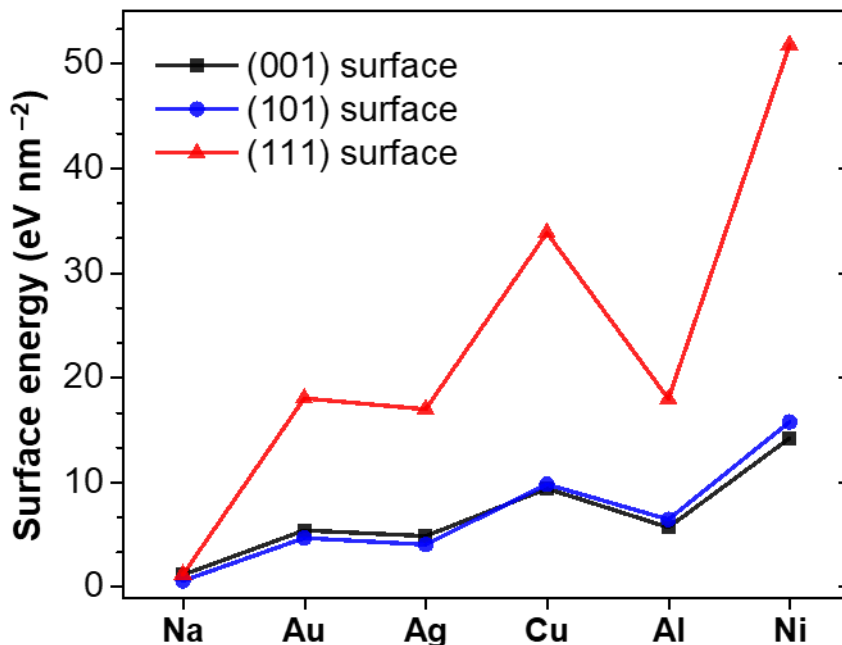


Figure 2.5 Surface energy of (001), (101), and (111) surfaces of pure metal systems.

calculations.^{52,53} In this study, the interface formation energy (E_{if}) of the interface system between sodium metal (Na) and the metal current collector (M) is defined as the energy difference between the total energy of the relaxed interface system and the energy of fully relaxed pure components. E_{if} can be calculated as follows:

$$E_{if} = E_{Na/M} - N_{Na}E_{Na} - N_{M}E_{M} ,$$

where the total energy of the fully relaxed interfacial model (with N_{Na} units of Na and N_{M} units of M) is denoted by $E_{Na/M}$. The energy per unit of the fully relaxed free pure Na and M bulk structures is denoted by E_{Na} and E_{M} , respectively. The interface formation energy defined based on this relation contains contributions from both the interfacial energy and elastic strain energy arising from the lattice mismatch between Na and the metal. The surface energies of pure sodium and metal were calculated based on the slab method by subtracting the total energy of the pure metal slab structure from the bulk system energy with the same number of atoms. The interaction between the surfaces of the slab can be disregarded because the slab thickness (10 Å) is sufficiently large. This can be represented by the following relationship:

$$\gamma = \frac{1}{2S} (E_{slab}^N - N \times E_{bulk}) ,$$

where the total energy of N units of the relaxed slab is denoted by E_{slab}^N , while the unit bulk total energy is expressed by E_{bulk} , the surface is denoted by S , and the coefficient 2 is used here because there are two equivalent surfaces in the surface model. The surface energy of each pure metal surfaces is shown in Figure 2.5.

Interfacial Energy

As discussed in the preceding section, the interface formation energy can be separated into two contributions, namely interfacial energy and strain energy. In order to evaluate the interfacial energy, the following procedures were utilized. The interface structures were subjected to full relaxation (atomic coordinates and cell-vector relaxations) to their external stress-free states, where $E_{Na/M}$ can be obtained. Subsequently, both Na and M bulk structures with the same shape and comparable atomic layer numbers, as used in the full relaxation step, were subjected to relaxation in the normal (z) direction (i.e., the in-plane (x and y) lattice parameters were kept fixed). Then, the interfacial energy was calculated through the following equation:

$$\sigma_{\text{Na/M}} = \frac{E_{\text{Na/M}(xyz)} - N_{\text{Na}}E_{\text{Na}(z)} - N_{\text{M}}E_{\text{M}(z)}}{2S} ,$$

where the fully-relaxed total energy of the interfacial structure is expressed by $E_{\text{Na/M}(xyz)}$. While the energy per atomic layer of the pure Na and M bulk structures after constrained relaxation, along the interface normal direction (z direction) with fixed x and y components of lattice parameters, is expressed by $E_{\text{Na}(z)}$ and $E_{\text{M}(z)}$, respectively. The atomic layer numbers of Na and M in the interfacial supercell is denoted by N_{Na} and N_{M} , respectively.

The work of adhesion (W_{ad}) of the interface is defined as the amount of energy required to separate the two surfaces from the interface reversibly.⁹ It can be calculated by subtracting interfacial energy from the two surfaces energy, as shown in the following relationship:

$$W_{\text{ad}} = \gamma_{\text{Na}} + \gamma_{\text{M}} - \sigma_{\text{Na/M}} ,$$

where γ_{Na} and γ_{M} denote the surface energies of Na and M from pure sodium and metal structure, respectively. $\sigma_{\text{Na/M}}$ is defined as the interfacial energy of sodium and metal interface.

Binding Energy: We constructed each metal pure surfaces and introduced Na atom at similar distance on each metal surface (Figure 1.7). Binding energy (E_{b}) between Na atom with each metal surfaces were calculated based on the following equation:

$$E_{\text{b}} = E_{\text{Na(1)/M}} - E_{\text{Na(1)}} - E_{\text{M}} ,$$

where $E_{\text{Na(1)/M}}$, $E_{\text{Na(1)}}$, and E_{M} are total energies of the Na-adsorbed metal surface, isolated Na atom, and metal surface, respectively.

Supplementary Note 1.

For the Na/Ni interface based on the thin film model that we adopt for our DFT calculation, it showed high W_{ad} but low E_{b} . This contrasting result can be attributed to the nature of Ni metal. Ni metal possesses high surface energy (Figure 2.5), this causes Na metal deposition on Ni surface to adopt island like formation (Figure 2.6). The thin film model which we imposed during our calculation limits the relaxation of Na metal on Ni substrate, thus resulting into higher surface energy than it supposed in the island deposition model. Assuming to take into account the natural behavior of Na metal deposition on Ni surface, the surface energy of Na island is lowered that the that of thin film as it is thermodynamically more favorable. Additionally, according to the island growth model criteria,

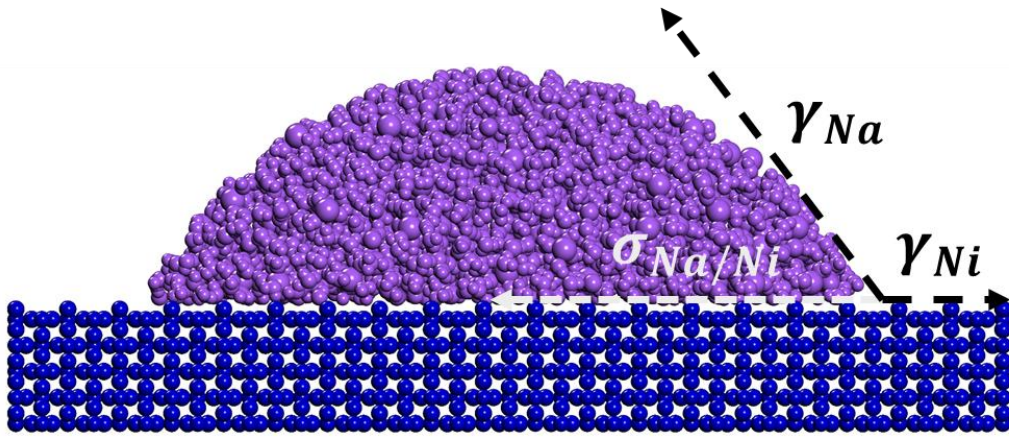


Figure 2.6 Island growth of Na metal deposition on Ni metal surface. γ_{Ni} is the surface energy of Ni metal (substrate), γ_{Na} is the surface energy of Na metal (crystal), and $\sigma_{Na/Ni}$ is the interfacial energy of the Na/Ni interface.

$$\gamma_{Ni} < \gamma_{Na} + \sigma_{Na/Ni} ,$$

where γ_{Ni} is the surface energy of Ni metal (substrate), γ_{Na} is the surface energy of Na metal (crystal), and $\sigma_{Na/Ni}$ is the interfacial energy of Na/Ni interface. Thus, the range of interfacial energy of Na/Ni interface can be expressed as follows:

$$\sigma_{Na/Ni} > (\gamma_{Ni} - \gamma_{Na}) .$$

Based on above equation and using the calculated surface energies of pure Na and Ni, the minimum interfacial energy was estimated to be $\sigma_{Na/Ni} = 13.05 \text{ eV nm}^{-2}$. By taking the limit of a Na atom bound on Ni surface as the lowest possible W_{ad} , the W_{ad} range of Na on Ni was calculated to be $0.06 \text{ eV nm}^{-2} < W_{ad} < 2.25 \text{ eV nm}^{-2}$, as shown in Figure 1.7.

2.4 Conclusions

In summary, we demonstrated a highly reliable seawater battery based on deterministic growth of the Na metal anode. Based on the different values of W_{ad} and E_b of metal surfaces with varying critical ratios of metal-pattern diameter and distance of pattern edges, we were able to obtain globally well-patterned growth of Na metal with enhanced cycling capability. Moreover, our approach is beneficial to improving the electrochemical performance of the anode-free seawater battery. The Coulombic efficiency and cycling capability were significantly increased by adopting the Cu/Al pre-patterned current collector, which clearly imply that deterministic growth of Na metal enhanced the seawater battery characteristics. We believe our strategy offers a new way to control Na metal plating on a current collector for anode-free batteries.

References

1. S. Yang, F. Zhang, H. Ding, P. he and H. Zhou, *Joule*, **2018**, 2, 1648.
2. Proactiveinvestors,
<https://www.proactiveinvestors.co.uk/companies/news/126693/macquarie-sees-lithium-as-the-new-wonder-resource-in-the-mining-sector-126693.html>, (accessed June 2016).
3. U.S. Geological Survey, Mineral Commodity Summaries 2012, Reston, VA, January, 2012.
4. P. Hartmann, C. L. Bender, M. Vračar, A. K. Dürr, A. Garsuch, J. Janek and P. Adelhelm, *Nat. Mater.*, **2013**, 12, 228.
5. M. D. Slater, D. Kim, E. Lee and C. S. Johnson, *Adv. Funct. Mater.*, **2013**, 23, 947.
6. N. Yabuuchi, K. Kubota, M. Dahbi and S. Komaba, *Chem. Rev.*, 2014, **114**, 11636.
7. J. Ding, H. Wang, Z. Li, K. Cui, D. Karpuzov, X. Tan, A. Kohandehghan and D. Mitlin, *Energy Environ. Sci.*, **2015**, 8, 941.
8. J. Park, C. W. Lee, J. H. Park, S. H. Joo, S. K. Kwak, S. Ahn and S. J. Kang, *Adv. Sci.*, **2018**, 5, 1801365.
9. J. K. Kim, E. Lee, H. Kim, C. Johnson, J. Cho and Y. Kim, *ChemElectroChem*, **2015**, 2, 328.
10. P. Manikandan, K. Kishor, J. Han and Y. Kim, *J. Mater. Chem. A*, **2018**, 6, 11012.
11. D. H. Kim, H. Choi, D. Y. Hwang, J. Park, K. S. Kim, S. Ahn, Y. Kim, S. K. Kwak, Y. J. Yu and S. J. Kang, *J. Mater. Chem. A*, **2018**, 6, 19672.
12. Y. Kim, G. T. Kim, S. Jeong, X. Dou, C. Geng, Y. Kim and S. Passerini, *Energy Storage Mater.*, **2019**, 16, 56.
13. S. Jeoung, S. H. Sahgong, J. H. Kim, S. M. Hwang, Y. Kim and H. R. Moon, *J. Mater. Chem. A*, **2016**, 4, 13468.
14. S. T. Senthilkumar, S. O. Park, J. Kim, S. M. Hwang, S. K. Kwak and Y. Kim, *J. Mater. Chem. A*, **2017**, 5, 14174.
15. D. H. Suh, S. K. Park, P. Nakhnivej, Y. Kim, S. M. Hwang and H. S. Park, *J. Power Sources*, **2017**, 372, 31.
16. Y. Zhang, J. S. Park, S. T. Senthilkumar and Y. Kim, *J. Power Sources*, **2018**, 400, 478.
17. W. Luo, C.-F. Lin, O. Zhao, M. Noked, Y. Zhang, G. W. Rubloff and L. Hu, *Adv. Energy Mater.*, **2017**, 7, 1601526.

18. Y. Zhao, L. V. Goncharova, Q. Zhang, P. Kaghazchi, Q. Sun, A. Lushington, B. Wang, R. Li and X. Sun, *Nano Lett.*, **2017**, 17, 5653.
19. A. Pei, G. Zheng, F. Shi, Y. Li and Y. Cui, *Nano Lett.*, **2017**, 17, 1132.
20. Y. Zhao, L. V. Goncharova, A. Lushington, Q. Sun, H. Yadegari, B. Wang, W. Xiao, R. Li and X. Sun, *Adv. Mater.*, **2017**, 29, 1606663.
21. C. Wang, H. Wang, E. Matios, X. Hu and W. Li, *Adv. Funct. Mater.*, **2018**, 28, 1802282.
22. D. Lin, Y. Liu and Y. Cui, *Nat. Nanotechnol.*, **2017**, 12, 194.
23. W. Luo, Y. Zhang, S. Xu, J. Dai, E. Hitz, Y. Li, C. Yang, C. Chen, B. Liu and L. Hu, *Nano Lett.*, **2017**, 17, 3792.
24. Y. Lu, Q. Zhang, M. Han and J. Chen, *Chem. Commun.*, **2017**, 53, 12910.
25. S.-S. Chi, X.-G. Qi, Y.-S. Hu and L.-Z. Fan, *Adv. Energy Mat.*, **2018**, 8, 1702764.
26. Y. Zhang, C. Wang, G. Pastel, Y. Kuang, H. Xie, Y. Li, B. Liu, W. Luo, C. Chen and L. Hu, *Adv. Energy Mat.*, **2018**, 8, 1800635.
27. B. Sun, P. Li, J. Zhang, D. Wang, P. Munroe, C. Wang, P. H. Notten and G. Wang, *Adv. Mater.*, **2018**, 30, 1801334.
28. G. Huang, J. Han, F. Zhang, Z. Wang, H. Kashani, K. Watanabe and M. Chen, *Adv. Mater.*, **2019**, 31, 1805334.
29. K. Yan, H. W. Lee, T. Gao, G. Zheng, H. Yao, H. Wang, Z. Lu, Y. Zhou, Z. Liang, Z. Liu, S. Chu and Y. Cui, *Nano Lett.*, **2014**, 14, 6016.
30. M. D. Tikekar, S. Choudhury, Z. Tu and L. A. Archer, *Nat. Energy*, **2016**, 1, 16114.
31. H. Wang, C. Wang, E. Matios and W. Li, *Nano Lett.*, **2017**, 17, 6808.
32. H. Lee, X. Ren, C. Niu, L. Yu, M. H. Engelhard, I. Cho, M. H. Ryou, H. S. Jin, H. T. Kim, J. Liu and W. Xu, *Adv. Funct. Mater.*, **2017**, 27, 1704391.
33. R. Xu, X.-Q. Zhang, X.-B. Cheng, H.-J. Peng, C.-Z. Zhao, C. Yan and J.-Q. Huang, *Adv. Funct. Mater.*, **2018**, 28, 1705838.
34. Y. Lu, Z. Tu and L. A. Archer, *Nat. Mater.*, **2014**, 13, 961.
35. Y. Lu, K. Korf, Y. Kambe, Z. Tu and L. A. Archer, *Angew. Chem., Int. Ed.*, **2014**, 53, 488.
36. Z. W. Seh, J. Sun, Y. Sun and Y. Cui, *ACS Cent. Sci.*, **2015**, 1, 449.
37. C. Yang, H. Xie, W. Ping, K. Fu, B. Liu, J. Rao, J. Dai, C. Wang, G. Pastel and L. Hu, *Adv. Mater.*, **2019**, 31, 1804815.
38. M. Ohring, *Materials Science of Thin Films*, Elsevier, San Diego, **2001**.

39. J.-I. Yamaki, S.-I. Tobishima, K. Hayashi, K. Saito, Y. Nemoto and M. Arakawa, *J. Power Sources*, **1998**, 74, 219.
40. W. Xu, J. Wang, F. Ding, X. Chen, E. Nasybulin, Y. Zhang and J.-G. Zhang, *Energy Environ. Sci.*, **2014**, 7, 513.
41. K. Yan, Z. Lu, H. W. Lee, F. Xiong, P.-C. Hsu, Y. Li, J. Zhao, S. Chu and Y. Cui, *Nat. Energy*, **2016**, 1, 16010.
42. H. Wang, Q. Zhang, H. Yao, Z. Liang, H. W. Lee, P.-C. Hsu, G. Zheng and Y. Cui, *Nano Lett.*, **2014**, 14, 7138.
43. E. Trofimov, O. Samoilova, O. Zaitseva and E. Vakhitova, *Metals*, **2018**, 8, 629.
44. Y. Kim, H. Kim, S. Park, I. Seo and Y. Kim, *Electrochim. Acta*, **2016**, 191, 1.
45. J. Han, S. M. Hwang, W. Go, S. T. Senthilkumar, D. Jeon and Y. Kim, *J. Power Sources*, **2018**, 374, 24.
46. S. J. Clark, M. D. Segall, C. J. Pickard, P. J. Hasnip, M. I. Probert and K. Refson, *Z. Kristallogr. Cryst. Mater.*, **2005**, 220, 567.
47. J. P. Perdew, K. Burke and M. Ernzerhof, *Phys. Rev. Lett.*, **1996**, 77, 3865.
48. D. Vanderbilt, *Phys. Rev. B*, **1990**, 41, 7892.
49. C. G. Broyden, *IMA J. Appl. Math.*, **1970**, 6, 76.
50. J. Barzilai and J. M. Borwein, *IMA J. Numer. Anal.*, **1988**, 8, 141.
51. H. J. Monkhorst and J. D. Pack, *Phys. Rev. B*, **1976**, 13, 5188.
52. Z. Liu, Y. Qi, Y. X. Lin, L. Chen, P. Lu and L. Q. Chen, *J. Electrochem. Soc.*, **2016**, 163, A592.
53. Y. Wang, Z.-K. Liu, L.-Q. Chen and C. Wolverton, *Acta Mater.*, **2007**, 55, 5934.
54. M. Benoit, C. Langlois, N. Combe, H. Tang and M.-J. Casanove, *Phys. Rev. B*, **2012**, 86, 075460.

